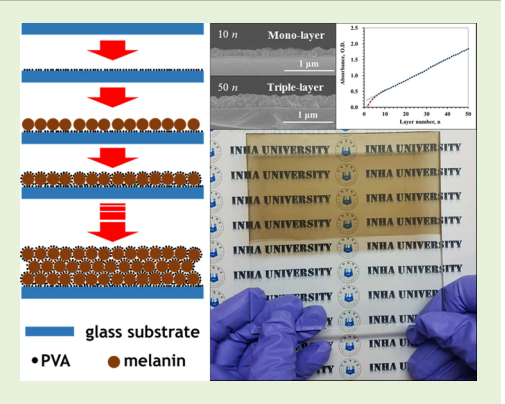


# Nanoarchitecturing of Natural Melanin Nanospheres by Layer-by-Layer Assembly: Macroscale Anti-inflammatory Conductive Coatings with Optoelectronic Tunability

Taesik Eom,<sup>†</sup> Kyungbae Woo,<sup>†</sup> Whirang Cho,<sup>§</sup> Jae Eun Heo,<sup>†</sup> Daseul Jang,<sup>†</sup> Jae In Shin,<sup>‡</sup> David C. Martin,<sup>§</sup> Jeong Jae Wie,<sup>‡</sup> and Bong Sup Shim<sup>\*,†</sup>

Supporting Information

ABSTRACT: Natural melanins are biocompatible conductors with versatile functionalities. Here, we report fabrication of multifunctional poly(vinyl alcohol)/melanin nanocomposites by layer-by-layer (LBL) assembly using melanin nanoparticles (MNPs) directly extracted from sepia officinalis inks. The LBL assembly offers facile manipulation of nanotextures as well as nmthickness control of the macroscale film by varying solvent qualities. The timeresolved absorption was monitored during the process and quantitatively studied by fractal dimension and lacunarity analysis. The capability of nanoarchitecturing provides confirmation of complete monolayer formation and leads to tunable iridescent reflective colors of the MNP films. In addition, the MNP films have durable electrochemical conductivities as evidenced by enhanced charge storage capacities for 1000 cycles. Moreover, the MNP covered ITO (indium tin oxide) substrates significantly reduced secretion of inflammatory cytokines, TNF- $\alpha$ , by



raw 264.7 macrophage cells compared to bare ITO, by a factor of 5 and 1.8 with and without lipopolysaccharide endotoxins, respectively. These results highlight the optoelectronic device-level tunability along with the anti-inflammatory biocompatibility of the MNP LBL film. This combination of performance should make these films particularly interesting for bioelectronic device applications such as electroceuticals, artificial bionic organs, biosensors, and implantable devices.

#### 1. INTRODUCTION

Biologically derived natural melanins are drawing attention for possible applications in bioelectronics such as implantable electrodes, interfaces for artificial organs, and biosensors due to their versatile functionalities including intrinsic conductivity and biocompatibility. Melanins are abundantly found in living creatures such as humans, mammals, fish, and microorganisms. Extracted melanins show intriguing physicochemical properties such as radical scavenging,<sup>1</sup> antioxidation,<sup>2,3</sup> electronic-ionic hybrid conductivities,<sup>4–10</sup> broadband light absorption,<sup>11–14</sup> metal ion chelating,<sup>15–18</sup> and redox activities. Depending on their molecular structures and functions, natural melanins are found in several different forms including eumelanin, pheomelanin, allomelanin, pyomelanin, and neuromelanin. The isolation of melanin from sepia officinalis (common cuttlefish) inks yields nanospheres mainly consisting of 98% eumelanin, which is enzymatically synthesized from 5,6dihydroxyindole-2-carboxylic acid (DHICA) and 5,6-dihydroxyindole (DHI) in organisms.<sup>20</sup> Although their exact molecular structure still remains elusive due to their insoluble stability in most solvents and relatively amorphous character, in silico modeling predicts that their molecules might be composed of a

few tens of stacks of heterogeneous DHI-DHICA planar oligomers. 21-23 These oligomer stacks are randomly aggregated with the support of binding proteins in a nominally spherical shape. 15,24 The aggregation forces originate from secondary intermolecular interactions including  $\pi$ - $\pi$  stacking, hydrogen bonding, and van der Waals forces, together providing extreme stability of the melanin nanoparticles (MNPs). The fabrication of MNP films has been reported by using solution drop casting, <sup>25</sup> spin coating, <sup>26-29</sup> pressed pellet packing, <sup>30,31</sup> polymeric blending, <sup>32,33</sup> and spray deposition. <sup>34</sup> However, it is still apparently limited owing to the difficulties in scaling up molecular-level functional structures to macro-scale films with well-defined thickness and properties.<sup>22</sup> Most recently, films using monodispersed synthetic polydopamine nanoparticles for structural coloring were reported via evaporation driven nanoparticle self-assembly on a vertical substrate<sup>35</sup> and the air/solution interface under static conditions.<sup>36</sup> Direct polymerizations on a substrate from melanin monomers including

Received: March 6, 2017 Revised: May 5, 2017 Published: May 16, 2017



<sup>&</sup>lt;sup>†</sup>Department of Chemical Engineering and <sup>‡</sup>Department of Polymer Science and Engineering, Inha University, 100 Inha-ro, Nam-gu, Incheon, Korea

<sup>§</sup>Department of Materials Science and Engineering, University of Delaware, 201 Du Pont Hall, Newark Delaware 19716, United States

dopamine, *L*-dopa, DHI, and DHICA are also suggested as another approach.<sup>37–39</sup> However, these methods are critically limited in achieving device-level assembly scale and coverage by utilizing rather irregular natural melanin particles.<sup>26,30,31,40–42</sup>

LBL assembly enables the fabrication of nm-thin films with tailored structures, compositions, and functionalities by easy and simple repeated depositions through intermolecular and hydrophobic interactions between polymers, nanomaterials, proteins, and viruses. <sup>43–49</sup> Thus, the assembly method has been widely used to fabricate highly stable, durable, and robust nanocomposites films with various shapes of nanomaterials including tubes, <sup>50–52</sup> platelets, <sup>12,53–55</sup> and spheres. <sup>56</sup> The uniqueness of the LBL process is the general tunability of the effective nanocomponent adsorption, leading to nearly perfect two-dimensional superstructures of nanomaterials. <sup>55</sup> However, LBL assembly has not been previously exploited for organizing natural MNPs because it is challenging to assemble meso- to microscale spherical particles by molecular precision. <sup>57</sup>

In this study, natural MNP films were successfully fabricated by the LBL process with poly(vinyl alcohol) (PVA). The LBL adsorption of MNPs with PVA could be readily controlled by the solvent qualities and the dipping conditions. We also demonstrated that the structural colors were gradually adjustable and that MNP stacks were precisely manipulated during the LBL nanoarchitecturing. The MNP coating on an ITO (indium tin oxide) electrode readily increased charge storage capacity (CSC) compared to a bare ITO. The natural MNP LBL films further showed significant anti-inflammatory behaviors by raw 264.7 macrophage cell tests for secreting a TNF- $\alpha$  cytokine.<sup>58</sup> This versatile combination of optical, electrical, and biological properties of the natural MNP LBL composites provides a unique multifunctional material option for biomedical applications such as bioorganic electronics, implantable devices, electroceuticals, and artificial bionic organs.

#### 2. EXPERIMENTAL SECTION

2.1. Preparation of Dipping Solutions. Natural MNPs were extracted from sepia officinalis (common cuttlefish) ink by washing with deionized water (DIW) and centrifugation at 3500 rpm for 10 min. The supernatant was removed after each run, and the final pellet was dried in a 60 °C oven overnight. Seventy-five milligrams of the collected powder was dispersed in 15 mL of DIW (0.5 wt %) and various cosolvents: 10 mL of DIW/5 mL of ethyl alcohol (EtOH, 99.0%; Daejung), 10 mL of DI/5 mL of methyl alcohol (MeOH, 99.0%; Daejung), 10 mL of DIW/5 mL of dimethyl sulfoxide (DMSO, 99.5%; Daejung), and 10 mL of DIW-5 mL of ammonia (NH<sub>3</sub>, 28-30%, Samchun chemicals). Poly(vinyl alcohol) (PVA; Mowiol 56–98, Aldrich) was dissolved in DIW (0.5 wt %) at 90 °C. All chemicals were used as received unless otherwise noted. An ELS-Z2 particle size analyzer (Otsuka) was utilized to measure the particle size and zetapotential of the MNPs in solvents. The shape of MNPs was observed by scanning electron microscope (SEM; SU8010, Hitachi) and fieldemission transmission electron microscopy (FE-TEM; JEM-2100F, Ieol)

**2.2. LBL Assembly on Glass Substrate.** Prior to LBL assembly of MNP films, a glass substrate was cleaned with MeOH by sonication. The substrate was first dipped in a PVA solution for 15 min, then washed by spraying DIW, and dried under mild air flow. MNPs were subsequently deposited onto the PVA-coated substrate after the incubation in each MNP solution for 15 min, followed by the same rinsing and drying procedures as described above. This dipping process was repeated until desired numbers of bilayers (*n*) were deposited. To monitor the effect of dipping time on the surface coverage of MNPs, the glass substrates were dipped in the MNP-dispersed aqueous solution at different time scales (3, 5, 20, 40 s and 1,

5, 10, 15, 20, 30 min). For deposition of bi- and trilayered MNP films, the LBL bilayer deposition process was repeated for 30 and 50 times, respectively.

**2.3. Structural Characterization of MNP LBL Film.** The degree of MNP loading in LBL assembled films was determined by UV—vis absorbance spectra in a Varian Cary 100 UV—vis spectrophotometer. The morphologies of the LBL-assembled MNP films were examined by SEM at a 15 kV accelerating voltage. To prevent electron charging, Pt was sputtered on the samples for 180 s. The surface coverage was calculated from image analysis of the SEM micrographs using ImageJ software by calculating ratio of the area occupied by adsorbed particles on the substrate to the total area of substrate. The top-surface topology of MNP films was analyzed by an n-tracer atomic force microscope (AFM; NanoFocus Inc.). AFM images with a scan area of 5  $\mu$ m × 5  $\mu$ m were obtained in tapping mode with a scanning rate of 0.4 Hz. The roughness of a MNP film was also measured from the AFM images.

The mechanical properties of the MNP film (10 n) were measured by nanoindentation technique (Nano indenter; G200, Keysight Technologies). The diamond tip (XP Berkovich Tip, 30  $\mu$ m in length, and 20 nm in radius) was applied by 50 nm in depth, and the modulus and the hardness were calculated in the range of 30–40 nm.

**2.4. Fractal Dimension Analysis of MNP LBL Film.** To briefly explain the fractal dimension analysis, SEM images were converted into binary images. The number of the neighbors connected to a particular position, N, was counted at different box size,  $\varepsilon$  (scaling factor). The fractal dimension is then calculated using the equation below by linear regression (least-squares) of  $\log N(\varepsilon)$  and  $\log \varepsilon$ :

$$D_{\rm F} = \lim_{\varepsilon \to 0} \frac{\log N(\varepsilon)}{\log \varepsilon}$$

where  $D_{\rm F}$  is the fractal dimension.<sup>59</sup>

**2.5. Macroscale MNP LBL Film.** To coat the MNP LBL film on a macro-scale substrate, a  $10 \text{ cm} \times 10 \text{ cm}$  glass substrate was used. As described, the substrate was alternately immersed in PVA (0.5 wt %) and melanin (0.5 wt %) solutions for 10 min with rinsing and drying.

**2.6. Electrochemical Property of MNP LBL Film.** To evaluate the electrochemical properties of the MNP LBL films, cyclic voltammetry (CV) was performed on indium tine oxide ITO-coated glass (ITO glass) substrate (1 cm  $\times$  2 cm) with a potentiostat (Reference 600, Gamry Instruments). The ITO glass was used in this experiment because it is a transparent and electrically conductive substrate. For every five-bilayers (5n) up to 20n, the CV data were collected in phosphate buffer saline (PBS) solution at a scan rate of 100 mV for the scanning voltage ranges of -0.2 to 0.8 V. Ag/AgCl was used as a reference electrode.

2.7. Cell Test by Raw 264.7 Cell and PC 12 Cell. Murine macrophage cells, raw 264.7, were grown with the 1 cm × 1 cm sized ITO samples on 24 well polystyrene plates. The cell culture media were prepared by mixing DMEM, FBS 10%, and pen strep 1%. The passage number and the concentration of seeded raw 264.7 cells in each well were 24 and  $2.6 \times 10^4$  cell/mL, respectively. The ITO samples were prepared by forming seven bilayers of MNP LBL coatings on ITO and by cleaning a bare ITO substrate. After seeding the cells on the ITO samples, they were cultured in CO2 incubator (5% CO<sub>2</sub>, 36 °C) for 24 h. The amount of TNF- $\alpha$  was quantified by TNF- $\alpha$  ELISA kit (KMC3011, Thermo Fisher Scientific Inc.) using cultured supernatant media. After every standard procedure of the ELISA kit, light absorbance at 450 nm wavelength was recorded using a microplate reader (iMark, Bio-Rad Laboratories). A concentration calibration curve of TNF-α was generated using 15.6-1000 pg/mL standard solutions included in the kit. The calculated concentration of TNF- $\alpha$  by the samples was averaged by repeated measurements from at least three different cell culture wells. PC12 cells were grown on MNP LBL coated, collagen coated, and bare polystyrene (PS) substrates. The cell culture media were prepared by mixing RPMI, FBS 10%, and pen strep 1%. The passage number and the concentration of seeded PC12 cells in each well were 23 and 1.0  $\times$  10<sup>4</sup> cell/mL,

respectively. They were cultured in  $CO_2$  incubator (5%  $CO_2$ , 36 °C) for 6 days.

#### 3. RESULTS AND DISCUSSION

**3.1. Solvent Effects on MNP Dispersions during LBL Assemblies.** Nanostructures of an LBL assembled film are governed by processing parameters such as dipping times, qualities of solutions, substrates, and LBL components, particularly, including surface charges, shapes, and sizes if they are nanomaterials. While their shape is mostly spherical, the size of MNPs dispersed in DIW was measured to be 142.4  $\pm$  38.7 nm by particle size analyzer (Figure 1). The  $\zeta$ -potentials

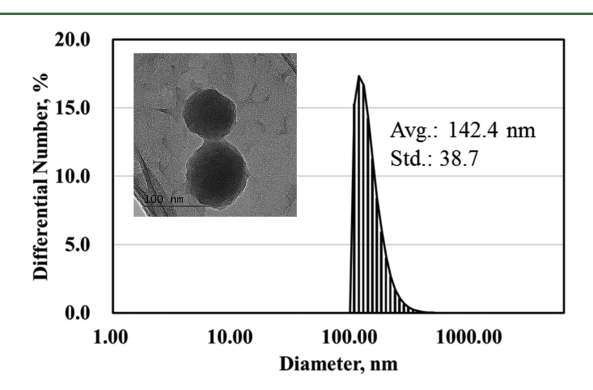


**Figure 1.** Particle size analysis of MNPs dispersed in DIW. Inset shows the TEM image of MNPs.

of MNPs in DIW, DIW-MeOH, DIW-NH<sub>3</sub>, DIW-EtOH, and DIW-DMSO were  $-37.0 \pm 0.1$ ,  $-18.2 \pm 0.5$ ,  $-36.9 \pm 0.5$ ,  $-12.1 \pm 1.3$ , and  $-14.5 \pm 0.9$  mV at 25 °C, respectively, as summarized in Table 1. The large negative  $\zeta$ -potential values of

Table 1. Zeta Potential Measurements of MNPs Dispersed in Various Solvents

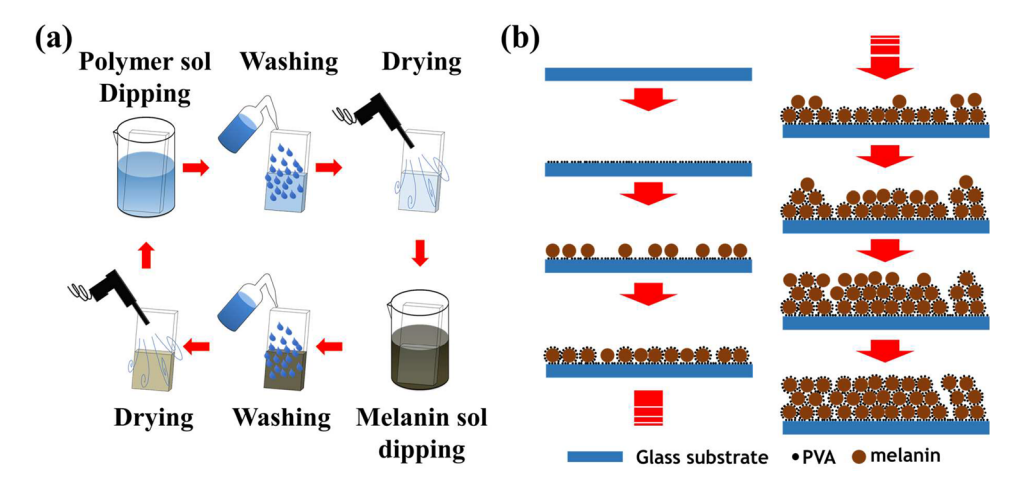
	zeta potential (mV)	pН
DIW	$-37.0 \pm 0.1$	5.50
DIW-MeOH	$-18.2 \pm 0.5$	5.30
DIW-NH <sub>3</sub>	$-36.9 \pm 0.5$	12.33
DIW-EtOH	$-12.1 \pm 1.3$	5.35
DIW-DMSO	$-14.5 \pm 0.9$	5.76

MNPs in DIW and DIW-NH $_3$  are indicative of thermodynamic stability of charge stabilized MNPs, originating from repulsion of electric double layer. Conversely, the  $\zeta$ -potentials in DIW-MeOH, DIW-EtOH, and DIW-DMSO imply that the surface charges of MNPs were only partially activated. Thus, slight precipitation over the course of several weeks was observed in DIW-MeOH, DIW-EtOH, and DIW-DMSO, but in DIW and DIW-NH $_3$ . While different degrees of sedimentational forces exist depending on solvent qualities and pHs, we assume that rigorous dispersion process right before LBL assembly was at least enough for comparing the adsorption efficiencies and LBL morphologies.

The LBL assembly of MNP was performed on a glass substrate by alternately dipping the substrate in the MNP dispersions and the PVA solutions. Scheme 1 shows the schematic process of the LBL assembly and their consequent LBL adsorption patterns of MNPs by the covering PVA layer. Because the size of melanin was much larger than the PVA layer thickness, only MNP adsorption patterns are observed, as if no binder is used at all. From previous observations, <sup>60</sup> PVA forms extremely thin layers, roughly less than 1 nm although it may vary with their molecular weights and layering conditions. Thus, the MNP dominates the optical behavior as well as the composition of the composite.

The adsorption pattern of MNPs also depends on the solvents of MNP dispersions. The MNP adsorption behaviors during LBL process were characterized by UV-vis light absorption spectra (Figure 2a-e). No characteristic peaks by the MNP LBL films were observed as that of the MNP solution. However, the MNP contents are readily distinguished by overall light absorbance levels. For comparing the LBL efficiencies, light absorbance at 300 nm by different MNP solvents are plotted against the number of LBL layers as shown in Figure 2f. Linear increments of absorbance during the layering processes were commonly observed regardless of the kind of solvent, which implies that the MNP stability was adequate. The differences between solvents were the slopes of light absorbance increments by repeating the dipping cycles. The MNPs in DIW showed the fastest increment, which implied that charge-transfer adsorption between MNPs and PVA is quite efficient. Thus, higher charges on MNPs resulted in faster adsorption on the noncharged PVA surface. For the case of MNPs in DIW-NH<sub>3</sub>, however, cationic NH<sub>4</sub><sup>+</sup> caused unnecessary charge-transfer competition with anionic MNPs

Scheme 1. Schematics of (a) Layer-by-Layer Assembly Processes and (b) Layering Patterns of [PVA/Melanin] LBL Films



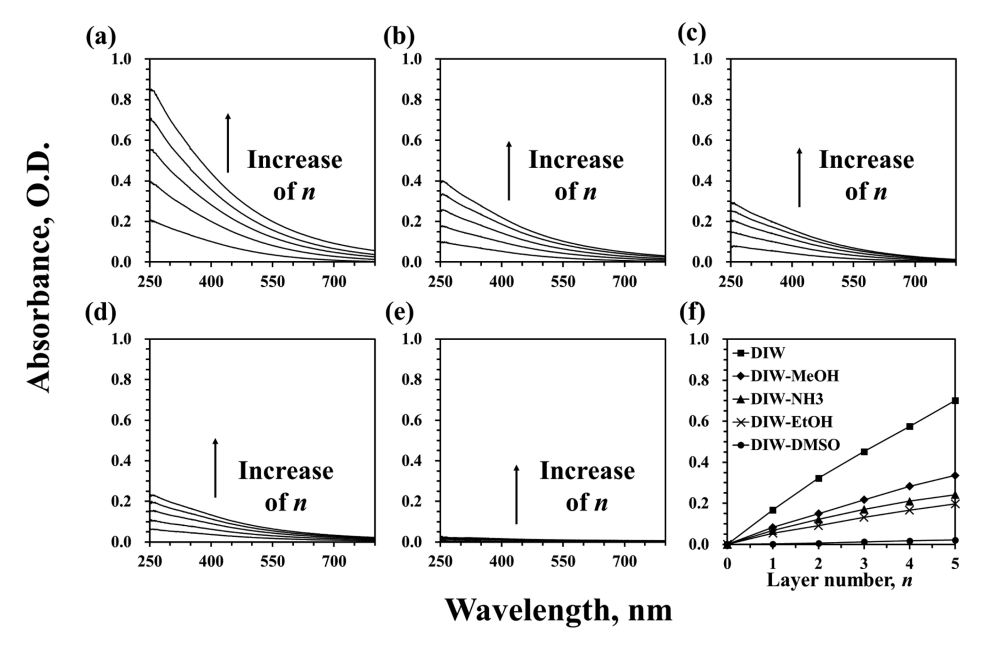


**Figure 2.** UV—vis light absorption spectra during MNP LBL assembly process. MNPs were dispersed in several different solvents such as (a) DIW, (b) DIW-MeOH, (c) DIW-NH<sub>3</sub>, (d) DIW-EtOH, and (e) DIW-DMSO. (f) Light absorption increments at 300 nm were plotted by increasing dipping cycles.

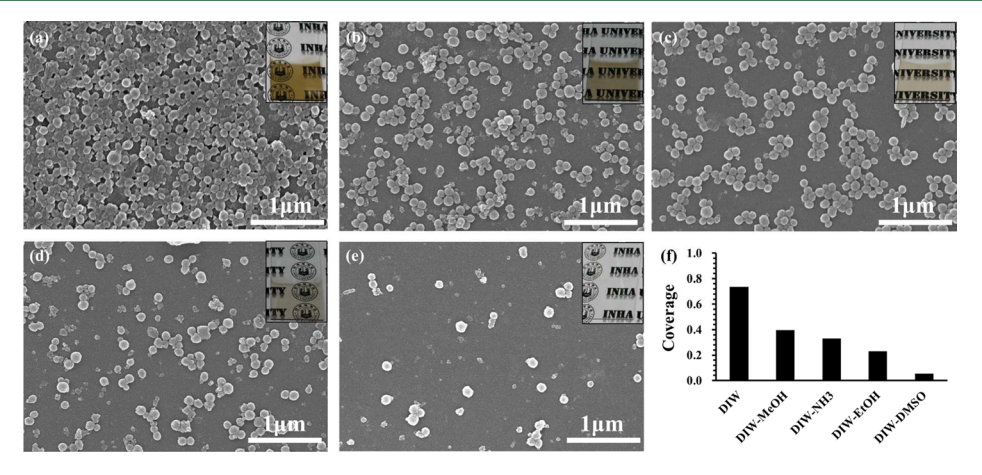
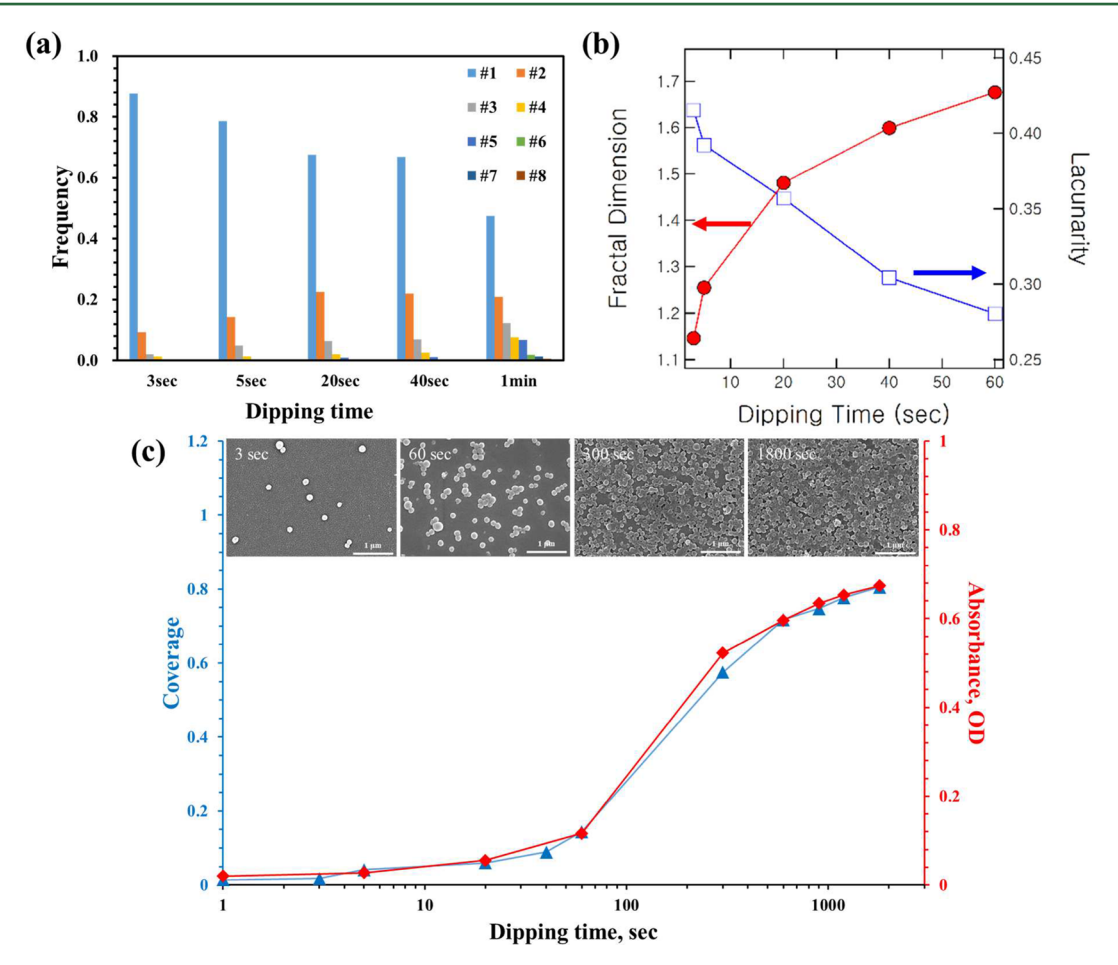


Figure 3. SEM images of MNP LBL assemblies (5n) from different MNP dispersions in (a) DIW, (b) DIW-MeOH, (c) DIW-NH3, (d) DIW-EtOH, and (e) DIW-DMSO. (f) Surface coverage comparison of these MNP LBL assemblies. (The logo is used with permission from Inha University.)

toward the neutral polar PVA surface. Thus, the high charge activation on MNPs in this case was not effectively translated to the effective MNP adsorption, unlike MNPs in DIW.

These adsorption increments were directly correlated to the surface coverage of MNPs on PVA, not forming aggregated MNPs. To further elucidate the MNP adsorption behavior, the deposited MNP LBL films were scrutinized by SEM micrographs. As shown in Figure 3, MNPs were uniformly deposited on the substrate by the LBL assembly. As in the UV-vis light absorbance comparison, the MNPs in DIW showed more complete surface coverage than the other series. Explaining these gradual variances requires an understanding of the dynamic intermolecular forces between LBL components as well as the solvent charge screening parameters. The attractive forces involved in these LBL assemblies include charge transfer, van der Waals, hydrogen bonding, and hydrophobic interactions. While each interaction potential contributes to form adsorbed layers, variances from the other may cause the differences in adsorbed amounts in each layer. As higher  $\zeta$ - potential can bring more effective charge transfer interactions between MNP and PVA, the order of the MNP adsorbed amounts roughly follows the magnitude of  $\zeta$ -potential. The van der Waals interaction also affects the LBL assembly differently in solvents, while the effective van der Waals interactions between MNPs and PVA after adsorption involve dielectric constants in solvents.<sup>61</sup> The dielectric constants of DIW, NH<sub>3</sub>, EtOH, MeOH, and DMSO at 20 °C are 80.4, 25, 24.5, 32.7, and 47, respectively. Thus, similar  $\zeta$ -potentials of MNPs in DIW and DIW-NH3 caused the differences in effective van der Waals interactions. The surface coverage MNPs in DIW was the highest among them. In addition, the difference of the dielectric constants between EtOH and MeOH resulted in higher coverage from MNPs in DIW-MeOH than those in DIW-EtOH. Furthermore, protic solvents can mediate hydrogen bonds in adsorbed states more effectively than aprotic ones. DMSO is polar aprotic, while MeOH and EtOH are polar protic. Thus, hydrogen bonding interactions between PVA and MNPs are severely disturbed by DMSO. For this reason, DIW-



**Figure 4.** (a) Frequency of MNP aggregations whose MNP counts vary from 1 to 8, as a function of dipping time. (b) Fractal dimension and lacunarity against dipping time for MNP LBL film. (c) Time-resolved monitoring of surface coverage and UV—vis absorbance at 300 nm wavelength by varying LBL dipping time of the 5*n* layered LBL films.

DMSO shows the most insignificant growth in MNP adsorption in LBL assemblies.

**3.2.** Kinetic Behaviors of MNP Adsorption during LBL Assemblies. To investigate the kinetics of MNP adsorption during LBL assembly at the early stages (5n), the dipping time in MNP solution was varied from 3, 5, 20, 40 s, and 1 min. The amount of adsorbed MNPs increased as the dipping time increased (SFigure 2). Initially, random absorption of individual MNPs lead to large interparticle distances and most MNPs were dispersed as single particles at 3 s of dipping, as shown in SFigure 2a. A small portion of MNPs formed 2 or 3 particle clusters even with 3 s dipping. The increased dipping time gradually decreased the fraction of individual MNPs, while the maximum particle number within the MNP cluster increased up to 8 at 1 min of dipping. A histogram of the number of particles within the MNP cluster is shown in SFigure 4a.

The adsorption pattern of MNPs was further quantitatively evaluated by means of fractal dimension analysis, which can represent the degree of complexity of the irregularly shaped objects. A fractal dimension of unity indicates a one-dimensional linear connectivity between objects, while completely filled two-dimensional planar objects have fractal dimension of two. As the LBL assembly of spherical MNPs inherently leaves void regions and cannot reach surface coverage of 2, fractal dimension between one and two is expected for MNPs. Also, the fractal dimension fluctuated at different locations and box size. This local distribution in

complexity can be visualized by constructing color-coded visual map of local connected fractal dimension.

The color-coded map demonstrates the increase in fractal dimension as a function of the LBL dipping time. At early stage, the dominant color-codes changed from red ( $D_F = 1.1-1.3$ ) to orange ( $D_F = 1.3-1.5$ ) and then yellow ( $D_F = 1.5-1.7$ ) as dipping time increased. Finally, yellow and green ( $D_F = 1.7-1.9$ ) were the majority color-codes after 1 min of the dipping time, indicating increased neighboring particles (SFigure 3). In addition to the local connected fractal dimension, the mean global fractal dimension was also quantified by a box counting method (see Experimental Section) to define an averaged value at each time mark. During the global fractal dimension calculation, lacunarity ( $\lambda$ , lacuna is gap in Latin) can be determined, which is the measure of heterogeneity:

$$\lambda = (CV)^2 = \left(\frac{\sigma}{\mu}\right)^2$$

where  $\lambda$  is the lacunarity, CV is the coefficient of variation,  $\sigma$  is the standard deviation, and  $\mu$  is the mean value.

Figure 4b shows the summarized global fractal dimension and lacunarity of MNPs. At 3 s dipping time, the average fractal dimension was measured to be 1.15. The increase in fractal dimension against dipping time shows fast saturation and 1.68 of fractal dimension was calculated at 1 min of the dipping time. In contrast to fractal dimension, lacunarity decreased as a

Biomacromolecules

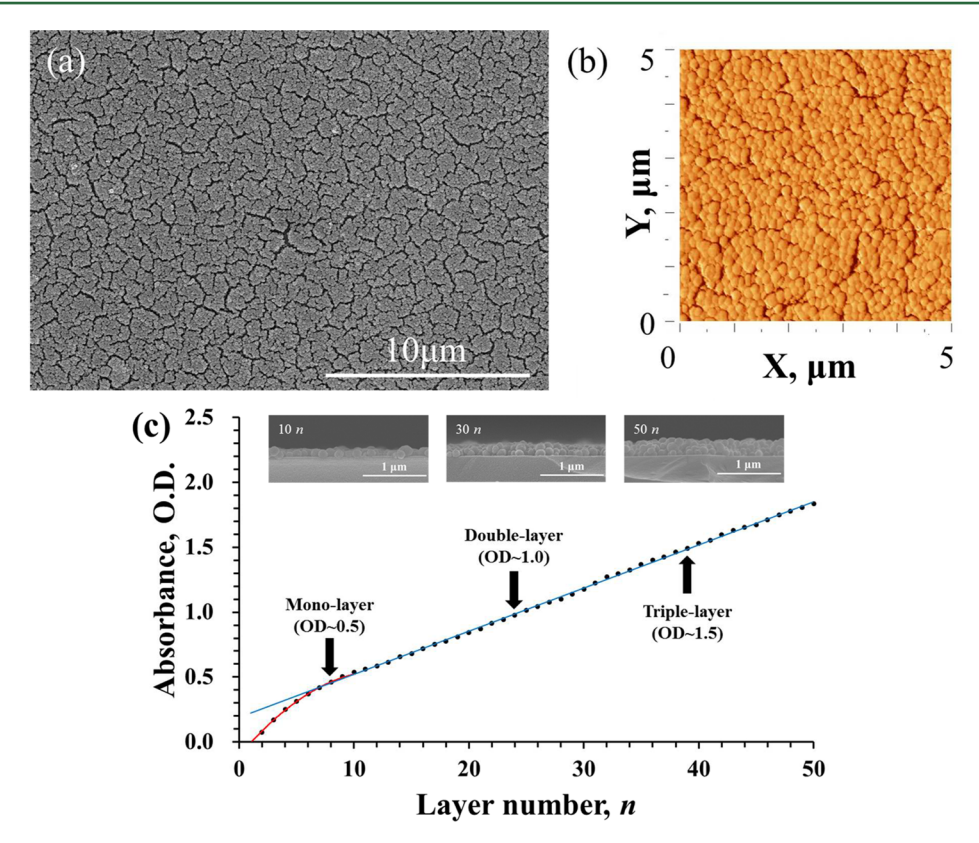


Figure 5. (a) SEM images of 50 layered MNP LBL film in top-view. (b) AFM image of a 50 n layered MNP LBL film. (c) Light absorbance trends at 300 nm during MNP LBL assemblies as increasing layering numbers.

function of dipping time, demonstrating random absorption behaviors of MNPs without nonuniformly deposited areas.<sup>59</sup>

3.3. Morphology of MNP LBL Composite Layers. The layered structure of MNP LBL film was also controlled by LBL deposition cycles. Cross-sectional images of the MNP LBL films were observed at every 10-bilayers (10n). The crosssectional coverage was calculated based on the triple-layered stack coverage, which corresponded to the 50-bilayered (50n) film (SFigure 4). Roughly, 10- and 25-bilayered films were equivalent with mono- and double-layer coverage, respectively. The cross-sectional SEM image revealed that the films were pretty uniform with film thickness around 300 nm. Layered structures were fully connected in the direction perpendicular to the surface over the almost entire film as shown in SFigure 4. If MNPs were fully stacked with hexagonal packing, the film thickness would be 367.5 nm with the particles of 142.4 nm in size. This deviation is attributed to nonhomogeneous particle size distribution and random particle packing during the LBL process. The morphology of the LBL films was examined by SEM and AFM. The top-view SEM image (Figure 5a) shows densely packed MNPs, which corroborated with the AFM phase image as shown in Figure 5b. The observation that the UV-vis absorbance of MNP films increased in every dipping cycles indicates that the adsorbed amount of MNP continuously increased up to 50 cycles without any failure (Figure 5c). Note that the growth rate of light absorbance was faster in the initial 10 cycles (10n) than that in the later cycles (over 10n). This rate change indicated that adsorption of MNPs on a bumpy MNP layer was more difficult than that on the smooth surface. Thus, the LBL of MNPs showed the higher adsorption before forming uniform monolayers, with slower adsorption after forming multiple stacked layers. In another sense, the

inflection point of the slope indicates the completion of forming MNP monolayer. This simple monitoring of the completion of MNP monolayer formation as well as multiple stacks is unique advantage in LBL assembly, which can not be easily achieved by other techniques.

The roughness of our MNP film was calculated from AFM measurements. The average roughness of the MNP LBL coated film was  $36.0 \pm 1.2$  nm. Considering the average diameters of MNPs to be  $142.4 \pm 38.7$  nm, the roughness of the coated film is surprisingly small. This smoothness is the unique result of molecular level assembly of the LBL process. Furthermore, this several 10 s scale roughness is upon the ideal levels of cell differentiation and proliferation, while a desirable level should vary by depending on cell sizes and phenotypes.  $^{62,63}$ 

The mechanical properties of MNP film were also estimated by nanoindentation measurement technique. The average modulus and hardness are  $5.3 \pm 3.4$  GPa and  $0.15 \pm 0.07$  GPa, repectively (Table 2). The maximum and minumum of

Table 2. Mechanical Strength of MNP Film

	modulus (GPa)	hardness (GPa)
average	$5.3 \pm 3.4$	$0.15 \pm 0.07$
max	11.4	0.29
min	2.1	0.08

modulus and hardness are quite different from 11.4 and 0.29 to 2.1 and 0.08 GPa (5.4 times in modulus and 3.6 times in hardness) depending on the tip positioning of nanoindenter. Considering that the MNP is a spherical particle and the roughness is around 36 nm, the contacted area of the tip will be significantly different from the top to the edges of the melanin

particle. Thus, the maximum values of this nanoindentation result possibly indicate the mechanical properties of melanin particle itself.

**3.4.** Iridescent Structural Colors of MNP LBL Films. When melanin-containing nanostructures were examined in reflected visible light, specific structural colors could be observed with conjunction of brown melanin pigments. For example, the iridescent colors of peacock feathers originate from structural interference of light through multistacked brown melanin pigments. <sup>64</sup> Here, the functions of melanin are provision of photonic structures and absorption of the stray light. <sup>40</sup> While photonic crystal structures from synthetic monodispersed spheres have been introduced, biomimetic structural colors with as-is natural melanin particles have not been preferably demonstrated due to the lack of structural controllability with rather irregular sized natural materials.

The iridescent structural colors have been successfully observed from artificial natural MNP films here for the first time by utilizing single particle-level structural tunability of the LBL assemblies (Figure 6). The nonreflective color gradually

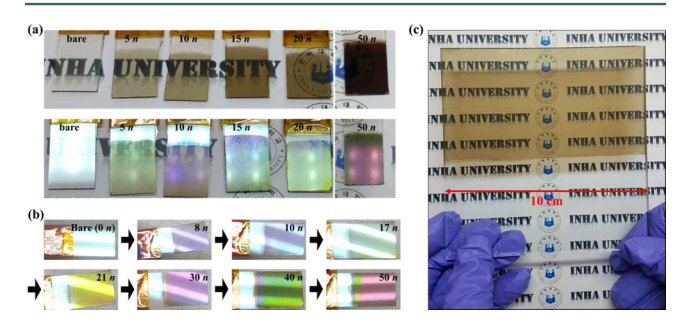


Figure 6. Structural colors of MNP LBL films. (a) Angle-dependent reflective colors of MNP LBL films and (b) reflective color changes (non  $\rightarrow$  purple  $\rightarrow$  blue  $\rightarrow$  green  $\rightarrow$  yellow  $\rightarrow$  red) with increasing layering numbers. (c) MNP LBL film assembled (10n) on a macroscale (10 cm  $\times$  10 cm) glass substrate. (The logo is used with permission from Inha University.)

changed from brown to dark brown with increasing LBL cycles. Photo images of the MNP LBL films showed a wide range of iridescent colors (purple, 8n; blue, 10n; green, 17n and 40n; yellow, 21n; and red, 30n and 50n) with increasing bilayer numbers as represented in Figure 6b. The reflective color was distinctively changed from 8n to 30n representing from purple to red, respectively, and this cycle was repeated after 30n. These colors originated from the MNP nanostructures that interfere with incident light. This structural coloration was clear and homogeneous throughout the entire surface. In addition, the MNP LBL film was uniformly fabricated on a macroscale glass substrate (10 cm × 10 cm). This demonstration suggests that the MNP LBL technique is easily extended to high throughput device production levels. Thus, the LBL assembly of MNPs has more flexible color controllability and larger uniformity in structural reflectance colors than previously reported methods. 35,36,40,65

**3.5. Electrochemical Performances of the MNP LBL Film.** The electrochemical activity of MNP LBL films was investigated using cyclic voltammetry (CV). The LBL deposition of MNPs up to 20*n* onto an ITO glass was further confirmed by the linear increase of UV–vis absorbance (SFigure 5b). The LBL films after every 5*n* were scanned by CV between –0.2 and 0.8 V at a rate of 100 mV. As shown in Figure 7, the charge storage capacity (CSC) grew from 0.69

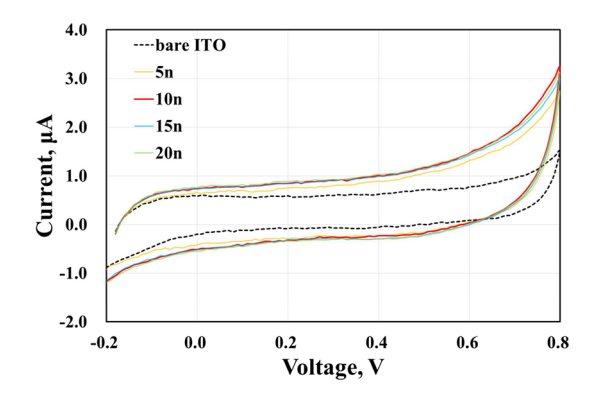


Figure 7. CV graphs of MNP LBL films assembled on ITO glasses.

μW for bare ITO to 1.07, 1.24, 1.23, and 1.28 μW for 5n, 10n, 15n, and 20n MNP LBL films, respectively. These increased CSCs for the LBL films are attributed to the electronic-ionic hybrid charge characteristic of MNPs that are closely related to the free radical content of MNPs. <sup>66</sup> The CSC value of the MNP films reached a plateau after 10n LBL deposition. Effective charge storage sites of the multiple stacked LBL films over 10n were not significantly different from the complete monolayered MNP films (10n) because active sites mostly exist on the surface. Ionic penetration through multiple layered MNP stacks seems not to be effective because dense particles as well as numerous charge trapping sites at the MNPs deteriorate ionic mobility throughout the films. Furthermore, electrical charge transport through the thickness direction of the LBL stacks was not very favorable due to insulating PVA layers between MNP stacks

For the electrochemical durability of the MNP LBL films, the CVs of a bare ITO and the MNP LBL films were carried out for 1000 cycles between -0.2 and 0.8 V at a scan rate of 100 mV (SFigure 5a). The UV-vis absorbance spectra of 20n MNP films before and after 1000 cycles of CV scans showed no apparent change, which indicates good stability of the MNP LBL films during the electrochemical testing. Although the CSCs of all the samples decreased after 1000 CV cycles, the MNP LBL films maintained higher CSC values than the bare ITO. Evidently, the MNP films are electrochemically more stable than even an ITO film.

3.6. Anti-inflammatory Responses and Biocompatibility by the MNP Films. Naturally existing MNPs are known to be biocompatible. However, the estimates of biocompatibility have been relatively qualitative, including evidence for cell attachment as well as the development of neuronal extensions. 32,36,42 Instead of estimating simple biocompatibility, we investigated whether the MNP films could quantitatively reduce inflammatory responses, which are thought to ultimately cause failures in implanted biomedical devices. Utilizing murine raw 264.7 macrophage cell lines, bare ITO and MNP LBL coated ITO were compared by how much immune initiating cytokine, TNF- $\alpha$ , was secreted. Because our melanin composites can compete with an ITO electrode in optoelectronic biodevice applications, the biocompatibility of ITOs as well as electrochemical performances has been compared. The quantified amounts of TNF- $\alpha$  produced by simply attaching the conductive surfaces were  $10.6 \pm 1.1$  and  $6.34 \pm 0.02$  pg/mL for the bare ITO and the MNP LBL coated ITO, respectively (see Figure 8). With lipopolysaccharide (LPS) activations, the TNF- $\alpha$  secretion became 528  $\pm$  79 and 109  $\pm$  9.98 pg/mL for the bare ITO and the MNP LBL coated ITO, respectively. Overall,

Biomacromolecules

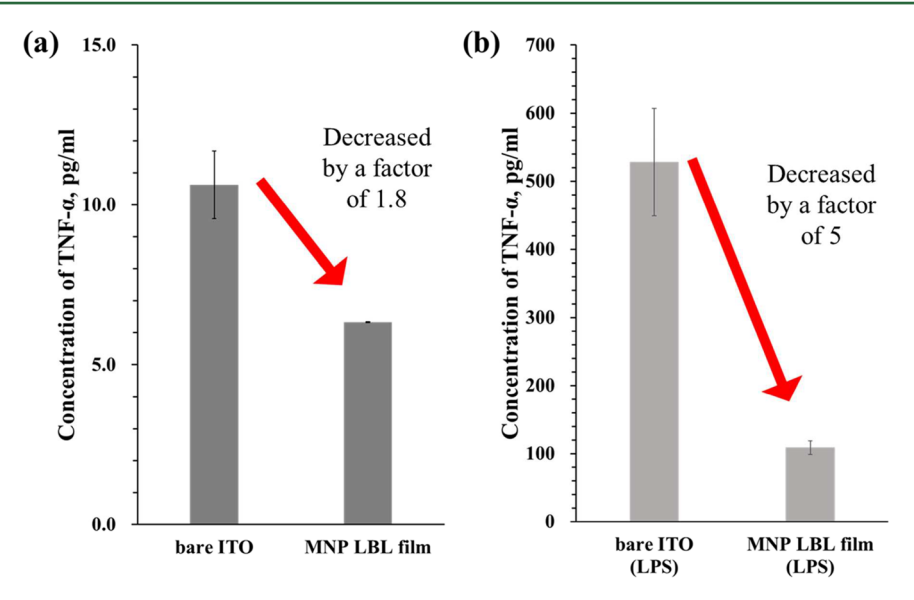


Figure 8. Concentration of TNF- $\alpha$  secreted by raw 264.7 cells on the ITO samples (a) without LPS and (b) with LPS. (a) bare ITO: 10.625  $\pm$  1.057 pg/mL and MNP LBL film on ITO: 6.338  $\pm$  0.019 pg/mL, (b) bare ITO with LPS: 528.216  $\pm$  78.936 pg/mL and MNP LBL film on ITO with LPS: 108.818  $\pm$  9.976 pg/mL.

the inflammatory cytokine secretion of a transparent ITO electrode has been reduced by a factor of 1.8 and 5 by coating MNP LBL films without and with LPS endotoxins, respectively.

PC 12 cells were also cultured on the MNP film and other control substrates. In 6 days, MNP film shows good cell attachment as well as PC12 neural differentiation compared to a bare PS slide and a collagen coated PS slide (SFigure 6). These results also suggest that the MNP films are not just safe enough for providing PC 12 neural cell cultures but also promotes the neural differentiation of PC 12 cells, which may be attributed to the electrical conductivity and the ideal roughness of the MNP LBL film. Not only biocompatibility, but also anti-inflammatory performances by the MNP films on ITO have been proved without much sacrificing transparency and even with improving electrochemical performances of an opto-electric ITO electrode.

# 4. CONCLUSIONS

We have introduced a new fabrication technique for creating natural MNP nanocomposite thin films via LBL assembly with PVA. The surface coverage, uniformity, and architectural structures of MNPs between mono- and multiple-stacks could be finely tuned by precisely controlling the MNP's adsorption behavior with varying dispersion media, dipping time, and number of LBL cycles. Among various solvents, deionized water yielded the most effective dispersion of the MNPs in terms of adsorption amounts as well as the film uniformity. Dipping time-resolved monitoring of MNP absorption process was conducted and quantitatively examined by using fractal dimension analysis. The rapid increase and saturation of fractal dimension indicated the fast formation of clustering at the monolayer level. Also, a decrease in lacunarity with dipping time supports random adsorption characteristic of MNPs. Fifty cycles of MNP LBL deposition resulted in densely packed triple-layers of MNP stacks whose regular nanoarchitecture produced structural iridescent reflective colors. The ability to control the number of LBL dipping cycles offered precise tunability of the iridescent colors over the entire visible light range from purple to red. In addition, macro-scale MNP LBL

film was successfully demonstrated on a 10 cm  $\times$  10 cm glass substrate. The MNP LBL films also demonstrated excellent electrochemical activity and durability, as confirmed by extending CSCs at 1000 cycles of CV scan compared to a bare ITO. In addition, the natural MNP LBL films have not only biocompatibility, but also anti-inflammatory protective performances on an abiotic ITO electrode. These biocompatible conductive nanocomposite films therefore suggest a unique optoelectronic materials option for the applications of bionic electronics, neural interfaces, and implantable devices.

## ASSOCIATED CONTENT

### S Supporting Information

The Supporting Information is available free of charge on the ACS Publications website at DOI: 10.1021/acs.bio-mac.7b00336.

SEM images of MNP LBL assemblies; color-coded maps of local connected fractal dimension; SEM images of MNP LBL films; thickness controllability of MNP LBL films; cyclic voltammetry of a MNP LBL film assembled on ITO glass; UV—vis absorbance spectra during layering of MNP LBL films on an ITO glass; PC12 cell attachments results (PDF)

#### AUTHOR INFORMATION

# **Corresponding Author**

\*E-mail: bshim@inha.ac.kr.

ORCID ®

David C. Martin: 0000-0003-1195-3838 Bong Sup Shim: 0000-0003-3205-6191

Notes

The authors declare no competing financial interest.

#### ACKNOWLEDGMENTS

This work was supported by INHA UNIVERSITY Research Grant, INHA UNIVERSITY World Class Smart Laboratory (WCSL) Research Grant, and by Basic Science Research Program through the National Research Foundation of Korea

(NRF-2017R1A2B4012736). D.C.M. acknowledges financial support from the University of Delaware and the National Science Foundation (DMR-1505144).

#### ABBREVIATIONS

MNP, melanin nanoparticle; PVA, poly(vinyl alcohol); LBL, layer-by-layer; ITO, indium tin oxide; TNF, tumor necrosis factor; DHICA, 5,6-dihydroxyindole-2-carboxylic acid; DHI, 5,6-dihydroxyindole; CSC, charge storage capacity; DIW, deionized water; EtOH, ethyl alcohol; MeOH, methyl alcohol; DMSO, dimethyl sulfoxide; SEM, scanning electron microscope; FE-TEM, field-emission transmission electron microscope; UV—vis, ultraviolet—visible; AFM, atomic force microscope; CV, cyclic voltammetry; PBS, phosphate buffer saline; DMEM, Dulbecco's modified Eagle medium; FBS, fetal bovine serum; ELISA, enzyme-linked immunosorbent assay; PS, polystyrene; RPMI, Roswell Park Memorial Institute

#### REFERENCES

- (1) Zou, Y.; Zhao, Y.; Hu, W. Chemical composition and radical scavenging activity of melanin from Auricularia auricula fruiting bodies. *Food Sci. Technol.* **2015**, 35 (2), 253–258.
- (2) Shanmuganathan, K.; Cho, J. H.; Iyer, P.; Baranowitz, S.; Ellison, C. J. Thermooxidative Stabilization of Polymers Using Natural and Synthetic Melanins. *Macromolecules* **2011**, *44* (24), 9499–9507.
- (3) Wang, D.; Chen, C.; Ke, X. B.; Kang, N.; Shen, Y. Q.; Liu, Y. L.; Zhou, X.; Wang, H. J.; Chen, C. Q.; Ren, L. Bioinspired Near-Infrared-Excited Sensing Platform for in Vitro Antioxidant Capacity Assay Based on Upconversion Nanoparticles and a Dopamine-Melanin Hybrid System. ACS Appl. Mater. Interfaces 2015, 7 (5), 3030–3040.
- (4) Osak, W.; Tkacz, K.; Czternastek, H.; Slawinski, J. I V characteristics and electrical conductivity of synthetic melanin. *Biopolymers* **1989**, 28 (11), 1885–1890.
- (5) Baraldi, P.; Capelletti, R.; Crippa, P. R.; Romeo, N. Electrical Characteristics and Electret Behavior of Melanin. *J. Electrochem. Soc.* **1979**, *126* (7), 1207–1212.
- (6) Mostert, A. B.; Powell, B. J.; Pratt, F. L.; Hanson, G. R.; Sarna, T.; Gentle, I. R.; Meredith, P. Role of semiconductivity and ion transport in the electrical conduction of melanin. *Proc. Natl. Acad. Sci. U. S. A.* **2012**, *109* (23), 8943–8947.
- (7) Ligonzo, T.; Ambrico, M.; Augelli, V.; Perna, G.; Schiavulli, L.; Tamma, M. A.; Biagi, P. F.; Minafra, A.; Capozzi, V. Electrical and optical properties of natural and synthetic melanin biopolymer. *J. Non-Cryst. Solids* **2009**, 355 (22–23), 1221–1226.
- (8) da Silva, M. I. N.; Deziderio, S. N.; Gonzalez, J. C.; Graeff, C. F. O.; Cotta, M. A. Synthetic melanin thin films: Structural and electrical properties. *J. Appl. Phys.* **2004**, *96* (10), 5803–5807.
- (9) McGinness, J.; Corry, P.; Proctor, P. Amorphous Semiconductor Switching in Melanins. *Science* **1974**, *183* (4127), 853–855.
- (10) Chen, C.-T.; Ball, V.; de Almeida Gracio, J. J.; Singh, M. K.; Toniazzo, V.; Ruch, D.; Buehler, M. J. Self-Assembly of Tetramers of 5,6-Dihydroxyindole Explains the Primary Physical Properties of Eumelanin: Experiment, Simulation, and Design. ACS Nano 2013, 7 (2), 1524–1532.
- (11) Grishchuk, V. P.; Davidenko, S. A.; Zholner, I. D.; Verbitskii, A. B.; Kurik, M. V.; Piryatinskii, Y. P. Optical absorption and luminescent properties of melanin films. *Tech. Phys. Lett.* **2002**, *28* (11), 896–898.
- (12) Capozzi, V.; Perna, G.; Carmone, P.; Gallone, A.; Lastella, M.; Mezzenga, E.; Quartucci, G.; Ambrico, M.; Augelli, V.; Biagi, P. F.; Ligonzo, T.; Minafra, A.; Schiavulli, L.; Pallara, M.; Cicero, R. Optical and photoelectronic properties of melanin. *Thin Solid Films* **2006**, *511*, 362–366.
- (13) Wolbarsht, M. L.; Walsh, A. W.; George, G. Melanin, a unique biological absorber. *Appl. Opt.* **1981**, 20 (13), 2184–2186.
- (14) Rosei, M. A.; Mosca, L.; Galluzzi, F. Photoelectronic properties of synthetic melanins. *Synth. Met.* **1996**, *76* (1–3), 331–335.

(15) Riley, P. A. Melanin. Int. J. Biochem. Cell Biol. 1997, 29 (11), 1235–1239.

- (16) Felix, C. C.; Hyde, J. S.; Sarna, T.; Sealy, R. C. Interactions of Melanin with Metal Ions. Electron Spin Resonance Evidence for Chelate Complexes of Metal Ions with Free Radicals. *J. Am. Chem. Soc.* 1978, 100 (12), 3922–3926.
- (17) Kim, D. J.; Ju, K. Y.; Lee, J. K. The Synthetic Melanin Nanoparticles Having An Excellent Binding Capacity of Heavy Metal Ions. *Bull. Korean Chem. Soc.* **2012**, *33* (11), 3788–3792.
- (18) Ju, K. Y.; Lee, J. W.; Im, G. H.; Lee, S.; Pyo, J.; Park, S. B.; Lee, J. H.; Lee, J. K. Bio-Inspired, Melanin-Like Nanoparticles as a Highly Efficient Contrast Agent for T-1-Weighted Magnetic Resonance Imaging. *Biomacromolecules* **2013**, *14* (10), 3491–3497.
- (19) d'Ischia, M.; Wakamatsu, K.; Napolitano, A.; Briganti, S.; Garcia-Borron, J.-C.; Kovacs, D.; Meredith, P.; Pezzella, A.; Picardo, M.; Sarna, T.; Simon, J. D.; Ito, S. Melanins and melanogenesis: methods, standards, protocols. *Pigm. Cell Melanoma Res.* **2013**, *26* (5), 616–633.
- (20) Liu, Y.; Simon, J. D. Isolation and biophysical studies of natural eumelanins: Applications of imaging technologies and ultrafast spectroscopy. *Pigm. Cell Res.* **2003**, *16* (6), 606–618.
- (21) d'Ischia, M.; Napolitano, A.; Pezzella, A.; Meredith, P.; Sarna, T. Chemical and Structural Diversity in Eumelanins: Unexplored Bio-Optoelectronic Materials. *Angew. Chem., Int. Ed.* **2009**, *48* (22), 3914–3921.
- (22) d'Ischia, M.; Napolitano, A.; Ball, V.; Chen, C. T.; Buehler, M. J. Polydopamine and Eumelanin: From Structure-Property Relationships to a Unified Tailoring Strategy. *Acc. Chem. Res.* **2014**, *47* (12), 3541–3550.
- (23) Arzillo, M.; Mangiapia, G.; Pezzella, A.; Heenan, R. K.; Radulescu, A.; Paduano, L.; d'Ischia, M. Eumelanin Buildup on the Nanoscale: Aggregate Growth/Assembly and Visible Absorption Development in Biomimetic 5,6-Dihydroxyindole Polymerization. *Biomacromolecules* **2012**, *13* (8), 2379–2390.
- (24) Clancy, C. M. R.; Simon, J. D. Ultrastructural organization of eumelanin from Sepia officinalis measured by atomic force microscopy. *Biochemistry* **2001**, *40* (44), 13353–13360.
- (25) Perna, G.; Lasalvia, M.; D'Antonio, P.; Mallardi, A.; Palazzo, G.; Fiocco, D.; Gallone, A.; Cicero, R.; Capozzi, V. Morphology of synthetic DOPA-eumelanin deposited on glass and mica substrates: An atomic force microscopy investigation. *Micron* **2014**, *64*, 28–33.
- (26) Bothma, J. P.; de Boor, J.; Divakar, U.; Schwenn, P. E.; Meredith, P. Device-quality electrically conducting melanin thin films. *Adv. Mater.* **2008**, *20* (18), 3539–3542.
- (27) Ambrico, M.; Ambrico, P. F.; Cardone, A.; Cicco, S. R.; Palumbo, F.; Ligonzo, T.; Di Mundo, R.; Petta, V.; Augelli, V.; Favia, P.; Farinola, G. M. Melanin-like polymer layered on a nanotextured silicon surface for a hybrid biomimetic interface. *J. Mater. Chem. C* **2014**, 2 (3), 573–582.
- (28) Piacenti da Silva, M.; Fernandes, J. C.; de Figueiredo, N. B.; Congiu, M.; Mulato, M.; de Oliveira Graeff, C. F. Melanin as an active layer in biosensors. *AIP Adv.* **2014**, *4* (3), 037120.
- (29) Wuensche, J.; Cicoira, F.; Graeff, C. F. O.; Santato, C. Eumelanin thin films: solution-processing, growth, and charge transport properties. *J. Mater. Chem. B* **2013**, *1* (31), 3836–3842.
- (30) Kim, Y. J.; Wu, W.; Chun, S.-E.; Whitacre, J. F.; Bettinger, C. J. Catechol-Mediated Reversible Binding of Multivalent Cations in Eumelanin Half-Cells. *Adv. Mater.* **2014**, *26* (38), 6572–6579.
- (31) Kim, Y. J.; Wu, W.; Chun, S.-E.; Whitacre, J. F.; Bettinger, C. J. Biologically derived melanin electrodes in aqueous sodium-ion energy storage devices. *Proc. Natl. Acad. Sci. U. S. A.* **2013**, *110* (52), 20912–20917.
- (32) Dong, W. F.; Wang, Y.; Huang, C. G.; Xiang, S. F.; Ma, P. M.; Ni, Z. B.; Chen, M. Q. Enhanced thermal stability of poly(vinyl alcohol) in presence of melanin. *J. Therm. Anal. Calorim.* **2014**, *115* (2), 1661–1668.
- (33) Wang, Y.; Li, T.; Wang, X. F.; Ma, P. M.; Bai, H. Y.; Dong, W. F.; Xie, Y.; Chen, M. Q. Superior Performance of Polyurethane Based on Natural Melanin Nanoparticles. *Biomacromolecules* **2016**, *17* (11), 3782–3789.

(34) Abbas, M.; D'Amico, F.; Morresi, L.; Pinto, N.; Ficcadenti, M.; Natali, R.; Ottaviano, L.; Passacantando, M.; Cuccioloni, M.; Angeletti, M.; Gunnella, R. Structural, electrical, electronic and optical properties of melanin films. *Eur. Phys. J. E: Soft Matter Biol. Phys.* **2009**, 28 (3), 285–291.

- (35) Xiao, M.; Li, Y. W.; Allen, M. C.; Deheyn, D. D.; Yue, X. J.; Zhao, J. Z.; Gianneschi, N. C.; Shawkey, M. D.; Dhinojwala, A. Bio-Inspired Structural Colors Produced via Self-Assembly of Synthetic Melanin Nanoparticles. *ACS Nano* **2015**, *9* (5), 5454–5460.
- (36) Wu, T. F.; Hong, J. D. Dopamine-Melanin Nanofilms for Biomimetic Structural Coloration. *Biomacromolecules* **2015**, *16* (2), 660–666.
- (37) Pop-Georgievski, O.; Popelka, S.; Houska, M.; Chvostova, D.; Proks, V.; Rypacek, F. Poly(ethylene oxide) Layers Grafted to Dopamine-melanin Anchoring Layer: Stability and Resistance to Protein Adsorption. *Biomacromolecules* **2011**, *12* (9), 3232–3242.
- (38) Strube, O. I.; Bungeler, A.; Bremser, W. Site-Specific In Situ Synthesis of Eumelanin Nanoparticles by an Enzymatic Autodeposition-Like Process. *Biomacromolecules* **2015**, *16* (5), 1608–1613.
- (39) Panzella, L.; Melone, L.; Pezzella, A.; Rossi, B.; Pastori, N.; Perfetti, M.; D'Errico, G.; Punta, C.; d'Ischia, M. Surface-Functionalization of Nanostructured Cellulose Aerogels by Solid State Eumelanin Coating. *Biomacromolecules* **2016**, *17* (2), 564–571.
- (40) Kohri, M.; Nannichi, Y.; Taniguchi, T.; Kishikawa, K. Biomimetic non-iridescent structural color materials from polydopamine black particles that mimic melanin granules. *J. Mater. Chem. C* **2015**, 3 (4), 720–724.
- (41) Araujo, M.; Viveiros, R.; Correia, T. R.; Correia, I. J.; Bonifacio, V. D. B.; Casimiro, T.; Aguiar-Ricardo, A. Natural melanin: A potential pH-responsive drug release device. *Int. J. Pharm.* **2014**, 469 (1), 140–145.
- (42) Bettinger, C. J.; Bruggeman, P. P.; Misra, A.; Borenstein, J. T.; Langer, R. Biocompatibility of biodegradable semiconducting melanin films for nerve tissue engineering. *Biomaterials* **2009**, *30* (17), 3050–3057.
- (43) Decher, G. Fuzzy nanoassemblies: Toward layered polymeric multicomposites. *Science* **1997**, 277 (5330), 1232–1237.
- (44) Kotov, N. A. Layer-by-layer self-assembly: The contribution of hydrophobic interactions. *Nanostruct. Mater.* **1999**, *12* (5–8), 789–796.
- (45) Ostrander, J. W.; Mamedov, A. A.; Kotov, N. A. Two modes of linear layer-by-layer growth of nanoparticle-polylectrolyte multilayers and different interactions in the layer-by-layer deposition. *J. Am. Chem. Soc.* **2001**, 123 (6), 1101–1110.
- (46) Wang, H. J.; Ishihara, S.; Ariga, K.; Yamauchi, Y. All-Metal Layer-by-Layer Films: Bimetallic Alternate Layers with Accessible Mesopores for Enhanced Electrocatalysis. *J. Am. Chem. Soc.* **2012**, *134* (26), 10819–10821.
- (47) Ariga, K.; Yamauchi, Y.; Rydzek, G.; Ji, Q. M.; Yonamine, Y.; Wu, K. C. W.; Hill, J. P. Layer-by-layer Nanoarchitectonics: Invention, Innovation, and Evolution. *Chem. Lett.* **2014**, 43 (1), 36–68.
- (48) Zakaria, M. B.; Malgras, V.; Takei, T.; Li, C. L.; Yamauchi, Y. Layer-by-layer motif hybridization: nanoporous nickel oxide flakes wrapped into graphene oxide sheets toward enhanced oxygen reduction reaction. *Chem. Commun.* **2015**, *51* (91), 16409–16412.
- (49) Zakaria, M. B.; Li, C. L.; Ji, Q. M.; Jiang, B.; Tominaka, S.; Ide, Y.; Hill, J. P.; Ariga, K.; Yamauchi, Y. Self-Construction from 2D to 3D: One-Pot Layer-by-Layer Assembly of Graphene Oxide Sheets Held Together by Coordination Polymers. *Angew. Chem., Int. Ed.* **2016**, 55 (29), 8426–8430.
- (50) Shim, B. S.; Zhu, J.; Jan, E.; Critchley, K.; Ho, S. S.; Podsiadlo, P.; Sun, K.; Kotov, N. A. Multiparameter Structural Optimization of Single-Walled Carbon Nanotube Composites: Toward Record Strength, Stiffness, and Toughness. ACS Nano 2009, 3 (7), 1711–1722.
- (51) Shim, B. S.; Chen, W.; Doty, C.; Xu, C. L.; Kotov, N. A. Smart Electronic Yarns and Wearable Fabrics for Human Biomonitoring made by Carbon Nanotube Coating with Polyelectrolytes. *Nano Lett.* **2008**, *8* (12), 4151–4157.

(52) Shim, B. S.; Kotov, N. A. Single-walled carbon nanotube combing during layer-by-layer assembly: From random adsorption to aligned composites. *Langmuir* **2005**, *21* (21), 9381–9385.

- (53) Podsiadlo, P.; Kaushik, A. K.; Arruda, E. M.; Waas, A. M.; Shim, B. S.; Xu, J. D.; Nandivada, H.; Pumplin, B. G.; Lahann, J.; Ramamoorthy, A.; Kotov, N. A. Ultrastrong and stiff layered polymer nanocomposites. *Science* **2007**, *318* (5847), 80–83.
- (54) Srivastava, S.; Kotov, N. A. Composite Layer-by-Layer (LBL) Assembly with Inorganic Nanoparticles and Nanowires. *Acc. Chem. Res.* **2008**, *41* (12), 1831–1841.
- (55) Tang, Z. Y.; Kotov, N. A.; Magonov, S.; Ozturk, B. Nanostructured artificial nacre. *Nat. Mater.* **2003**, 2 (6), 413–U8.
- (56) Vial, S.; Pastoriza-Santos, I.; Perez-Juste, J.; Liz-Marzan, L. M. Plasmon coupling in layer-by-layer assembled gold nanorod films. *Langmuir* **2007**, 23 (8), 4606–4611.
- (57) Liu, B.-T.; Yeh, W.-D. Antireflective surface fabricated from colloidal silica nanoparticles. *Colloids Surf., A* **2010**, 356 (1-3), 145–149
- (58) Panilaitis, B.; Altman, G. H.; Chen, J. S.; Jin, H. J.; Karageorgiou, V.; Kaplan, D. L. Macrophage responses to silk. *Biomaterials* **2003**, 24 (18), 3079–3085.
- (59) Pantic, I.; Harhaji-Trajkovic, L.; Pantovic, A.; Milosevic, N. T.; Trajkovic, V. Changes in fractal dimension and lacunarity as early markers of UV-induced apoptosis. *J. Theor. Biol.* **2012**, *303*, 87–92.
- (60) Shim, B. S.; Tang, Z. Y.; Morabito, M. P.; Agarwal, A.; Hong, H. P.; Kotov, N. A. Integration of conductivity transparency, and mechanical strength into highly homogeneous layer-by-layer composites of single-walled carbon nanotubes for optoelectronics. *Chem. Mater.* **2007**, *19* (23), 5467–5474.
- (61) Jung, B. G.; Min, S.-H.; Kwon, C.-W.; Park, S.-H.; Kim, K.-B.; Yoon, T.-S. Colloidal Nanoparticle-Layer Formation Through Dip-Coating: Effect of Solvents and Substrate Withdrawing Speed. *J. Electrochem. Soc.* **2009**, *156* (5), K86–K90.
- (62) Gittens, R. A.; McLachlan, T.; Olivares-Navarrete, R.; Cai, Y.; Berner, S.; Tannenbaum, R.; Schwartz, Z.; Sandhage, K. H.; Boyan, B. D. The effects of combined micron-/submicron-scale surface roughness and nanoscale features on cell proliferation and differentiation. *Biomaterials* **2011**, 32 (13), 3395–3403.
- (63) Zareidoost, A.; Yousefpour, M.; Ghaseme, B.; Amanzadeh, A. The relationship of surface roughness and cell response of chemical surface modification of titanium. *J. Mater. Sci.: Mater. Med.* **2012**, 23 (6), 1479–1488.
- (64) Chung, K.; Yu, S.; Heo, C.-J.; Shim, J. W.; Yang, S.-M.; Han, M. G.; Lee, H.-S.; Jin, Y.; Lee, S. Y.; Park, N.; Shin, J. H. Flexible, Angle-Independent, Structural Color Reflectors Inspired by Morpho Butterfly Wings. *Adv. Mater.* **2012**, 24 (18), 2375–2379.
- (65) Zhang, Y. F.; Dong, B. Q.; Chen, A.; Liu, X. H.; Shi, L.; Zi, J. Using Cuttlefish Ink as an Additive to Produce Non-iridescent Structural Colors of High Color Visibility. *Adv. Mater.* **2015**, 27 (32), 4719–4724.
- (66) Rienecker, S. B.; Mostert, A. B.; Schenk, G.; Hanson, G. R.; Meredith, P. Heavy Water as a Probe of the Free Radical Nature and Electrical Conductivity of Melanin. *J. Phys. Chem. B* **2015**, *119* (48), 14994–15000.